3-1-2022

Characterizing fiber-matrix debond and fiber interaction mechanisms by full-field measurements

Robert Livingston
Rowan University

Behrad Koohbor
Rowan University

Recommended Citation

Robert Livingston, Behrad Koohbor. Characterizing fiber-matrix debond and fiber interaction mechanisms by full-field measurements. Composites Part C: Open Access, Volume 7, March 2022, 100229.

Composites Part C: Open Access 7 (2022) 100229

Contents lists available at ScienceDirect

Composites Part C: Open Access

journal homepage: www.sciencedirect.com/journal/composites-part-c-open-access

Characterizing fiber-matrix debond and fiber interaction mechanisms by full-field measurements

Robert Livingston, Behrad Koohbor *

Department of Mechanical Engineering, Rowan University, 201 Mullica Hill Rd., Glassboro, NJ 08028, United States of America

ARTICLE INFO

Keywords:
Polymer-matrix composites
Debonding
Failure
Digital image correlation

ABSTRACT

An experimental approach is developed and utilized to characterize the fiber-matrix interfacial debonding mechanism and its effect on matrix cracking in unidirectional (UD) fiber composites. Local deformation response at the fiber-matrix interface is first studied by analyzing the strain fields developed in the vicinity of macro fibers in single-fiber samples. A practical approach for the identification of normal cohesive behavior at the fiber-matrix interface is presented and implemented in a finite element model that replicates the experimental findings. Fiber-to-fiber interaction, debond formation, and failure mechanisms in multiple fiber systems are then studied by varying the distance and angle between adjacent fibers in double-fiber samples. The experimental results indicate that the spacing and angular orientation between adjacent fibers affect the interface debond initiation and propagation, as well as subsequent matrix failure mechanisms. It is also shown that compared with fiber spacing, angular distance has a more significant effect on matrix cracking in UD composites under transverse tension. Results presented in this work provide an experimental-based quantitative insight into the mechanics of fiber-matrix interface using *in-situ* full-field measurements.

1. Introduction

Fiber-matrix Interfacial debond is the first form of damage that occurs in fiber composites subjected to transverse tension. This type of damage initiates at far-field stresses well below the tensile strength of both fiber and matrix materials [1]. Upon increasing the tensile load, the debonded zone propagates circumferentially along the fiber-matrix interface and then kinks out inside the matrix. The coalescence of these kinked-out microcracks leads to the development of larger cracks that proliferate rapidly throughout the entirety of the lamina, causing through-thickness cracks in transverse plies. Upon reaching interlaminar regions, these transverse cracks can lead to delamination, fiber breakage, and eventually complete separation [2]. Therefore, due to its substantial impact on the failure behavior of fiber-reinforced composites, characterizing the mechanics of the fiber-matrix interfacial debonding process is significant.

Revealing the underlying mechanisms associated with fiber-matrix interface failure, as the origin of transverse cracking in fiber composites, has been the topic of numerous analytical and modeling studies. Specifically, finite element analyses that are based on energy release rate (ERR) calculations and the cohesive response of the fiber-matrix interface have gained tremendous attention in the past decade [2–9]. Micromechanics simulations developed based on realistic composite structures with dense fiber packings suggest that non-uniform spatial distribution of fibers, local constraints imposed by the adjacent laminae, manufacturing-induced voids and microcracks, and residual stresses developed due to post-cure processes can affect the fiber-matrix debonding and transverse cracking mechanisms in composites [10–12]. Regardless of the specific methodology, computational studies of matrix cracking phenomena suggest that the likely sites of fiber-matrix debonding are in fiber clusters where the local stress fields attain high peaks. Therefore, the role of neighboring fibers becomes an important factor in predicting the initiation and progression of matrix cracking in UD composites.

Although proven extremely useful in addressing some of the fundamental questions, a great majority of the available modeling predictions lack proper experimental validations. Besides, there still exist fundamental gaps in the understanding of the mechanisms associated with the fiber-to-fiber interaction in terms of crack kinking, microcracks coalescence, and transverse crack formation. An example of such gaps is the common assumption that the link between kinked-out microcracks is always established between the nearest-neighbor fibers [8, 13-15].

* Corresponding author.
E-mail address: koohbor@rowan.edu (B. Koohbor).

https://doi.org/10.1016/j.jcomc.2022.100229
Received 13 September 2021; Received in revised form 23 November 2021; Accepted 4 January 2022
Available online 7 January 2022

While such assumptions seem acceptable for numerical approximation, experimental evidence to support them is rare. The limited experimental evidence in this active area of research is due to the highly hierarchical and multiscale nature of transverse cracking in fiber composites. The fact that the nucleation of fiber-matrix interfacial debonding at sub-micron scales progresses into micrometer cracks and then into larger cracks that run across several hundred micrometer thickness of a lamina hinders the design of proper experimental approaches that can capture the true nature of these failure mechanisms. Therefore, most experimental studies in this area are limited to either overly simplified tests wherein stress/strain states are inconsistent with the actual phenomenon, or measurements performed at length scales that are orders of magnitude different from those at which the failure phenomena take place.

Experimental investigations conducted to study the fiber-matrix interface debonding mechanisms are mostly focused on methods that enable the characterization of interface strength under *shear loading*. Among those are micromechanical tests wherein external load is applied directly on the fiber, such as pull/push out, microbond, and three-fiber tests, or those in which the external load is applied on the matrix, *e.g.*, fragmentation and single-fiber Broutman tests [16, 17]. Some of these test methods, *e.g.*, microbond (microdroplet) tests, have been modified to allow for measurements at high strain rate conditions as well [18, 19]. Despite certain achievements in the design of experiments that allow for the characterization of interfacial shear properties, there has been a clear lack of measurement methods to characterize the interface mechanics under normal loading conditions. Among the limited experimental studies carried out in this area, measurements facilitated by 3D *in situ* microtomography have provided useful quantitative information on nature and multi-stage damage evolution mechanisms at the fiber-matrix interface in single fiber samples [20]. Nevertheless, these micro-tomography experiments are reported to be limited by the X-ray image resolution, long interframe intervals, and the loading capacity of the built-in tensile frames. Besides, low contrast and the susceptibility of polymer matrix damage due to exposure to X-ray beam are also among the less significant challenges in tomography-assisted experiments [21, 22].

The development of high magnification full-field measurement techniques, especially digital image correlation (DIC), has provided new opportunities for accurate experimental characterization of material behavior at dissimilar interfaces and over a broad spectrum of length scales. Recent advancements in this powerful technique have proven useful especially in multiscale characterization of composites [23–25]. A perfect example of such multiscale measurements made possible by high magnification optical and/or scanning electron microscope (SEM) DIC is the micromechanics characterization of the fiber-matrix interface in transversely loaded composites. For instance, strain mapping in the vicinity of fibers in both polymer-matrix [26–28] and ceramic-matrix [23] fiber-reinforced composites have been successfully conducted by SEM DIC. The discontinuous nature of image reconstruction in SEM along with adverse e-beam charging effects have been identified as the two major challenges associated with SEM DIC analysis of fiber composites. On the other hand, high magnification optical DIC has been successfully utilized in a number of recent studies to uncover interfacial damage mechanisms in single-fiber samples under transverse tensile loads. For example, a series of recent studies by Tabiai *et al.* [29–31] proved that high magnification optical DIC measurements carried out on single PTFE macro-fiber (fiber diameter ~1 mm) composite samples can lead to an accurate assessment of displacement and strain fields in the fiber vicinity. This data can then be used to identify the three steps associated with the interface damage evolution, *i.e.*, an initial symmetric debonding formed at diagonally opposite locations at the interface, followed by crack growth along the interface, and finally, matrix failure caused by a crack kinking process [29]. These studies were later expanded to include several different fiber-matrix systems. It was also documented that as long as full-field measurements are conducted properly, the fiber size effects are insignificant, at least for fundamental studies performed on macro fibers with diameters ranging from a few hundred micrometers to 1 mm [30]. Based on these measurements, a combined DIC-image processing technique was recently developed to facilitate autonomous and rapid detection of the interface debond and subsequent matrix cracking phenomena [31].

Although the potential applications and versatile capabilities of DIC in the analysis of fiber-matrix interface mechanics have become evident, there still exist certain gaps in the practical approaches that allow for establishing quantitative correlations between global and local stress and deformation fields from an experimental perspective. The present study aims to develop an experimental approach that can be useful in addressing the following specific questions: (1) How can full-field measurements be used to correlate global stress and strains with the local deformation fields developed in the fiber vicinity in an epoxy matrix, and (2) How do fiber spacing and orientation alter these local strain fields? Although there exist numerous *modeling and numerical* studies that address these questions with great detail, the present study is unique in providing an *experimental* insight into the mechanics of fiber-matrix interface by *in-situ* full-field measurements. To this end, composite samples with one and two glass macro fibers are fabricated and subjected to transverse tension. Optical DIC is used to analyze the local deformation fields, while also providing data to calibrate finite element models. Results obtained from single-fiber tests are used to explain the fundamental mechanisms of interface debond nucleation and propagation. although similar measurements on model composites with micrometric fibers are available [26], the nature of electron microscopy imaging used in those studies does not allow for the characterization of debonding and matrix failure during continuous loading conditions. Full-field measurements are also performed on double-fiber samples wherein the distance and angular orientation of the two macro fibers are varied systematically. Results from these measurements are then used to characterize the interactions between adjacent fibers. The combination of full-field measurements and finite element analyses performed in this work all for the study of some of the fundamental mechanisms associated with the sources of microcrack coalescence and transverse crack formation in UD composites. Furthermore, the results provided in this work can be used directly for the verification of model-based predictions.

2. Experimental methods

2.1. Materials and sample preparation

Single fiber samples were prepared by embedding a single glass macro fiber (borosilicate clear glass, 2 mm diameter, McMaster-Carr, USA) in a thermoset epoxy resin (two-component clear epoxy resin, ProMarine Supplies Co., MI, USA). Macro fibers were used in this work to facilitate high magnification optical measurements. Note that the use of macro fibers for experimental characterization of the fiber-matrix interface was justified in previous studies [29, 30]. Borosilicate glass macro fibers were used in this work due to similarities between their mechanical properties and those of E-glass fibers. The matrix material used in this work was a proprietary clear thermoset resin curable at room temperature. The room temperature curable resin was selected to minimize the unfavorable effects due to the mismatch between the coefficients of thermal expansions (CTE) of fiber and matrix materials [32]. When cured in high temperature conditions, such CTE mismatch can lead to the development of residual stresses at the fiber-matrix interface. Mechanical properties of the glass macro fibers and epoxy matrix are listed in Table 1. More details about the mechanical characterization of the polymer matrix can be found in **Supplementary Information**.

The uncured monomer was cast into a silicone dog-bone mold. The silicone mold was pre-fabricated with dimensions in accordance with ASTM D638 after [30]. The glass fibers were prepared by sanding one

Table 1-
Mechanical properties of the matrix and fiber materials used in this work.

Material	Elastic Modulus (GPa)	Poisson's ratio	Yield strength (MPa)	Tensile strength (MPa)	Failure strain, ε_f	Density (kg/m^3)
Epoxy*	2.36 ± 0.10	0.40 ± 0.04	31.70 + 1.12	45.25 ± 0.74	0.035 ± 0.001	1065
Glass Fiber**	63	0.3	–	–	–	2214

* Based on 3 independent in-house measurements.
** Data provided by the manufacturer.

end with 240 grit sandpaper to ensure a flat end and proper penetration into the monomer while curing. Prior to insertion into the resin, the glass fiber piece was cleaned with isopropanol to remove any unwanted substance on the surface. The unsized glass fiber piece was then inserted into and held perpendicular inside the uncured resin with the aid of a 3D printed jig. Custom jigs were 3D printed out of ABS with one (for single-fiber samples) and two (for double-fiber samples) holes to facilitate keeping the glass fibers in position during the epoxy curing period (see Fig. 1a). The epoxy was cured for 48 h at room temperature. After curing, the front (camera-facing) surface of the sample was lightly polished with fine sandpaper to remove any imperfections and also to ensure the glass fiber section is aligned with the surface of the sample. A similar approach was followed to prepare double-fiber samples. As shown in Fig. 1, the inter-fiber spacing, d, and the angular distance, α, between the fibers in double-fiber samples were varied. Double fiber samples with nominal inter-fiber spacings of 0.6ϕ, 2ϕ, and 3ϕ (ϕ denotes fiber diameter) and nominal angles of 0°, 30°, 45°, 60°, 90° relative to the horizontal were prepared and tested. Table 2 lists the nominal and measured values of inter-fiber spacing and angles. The discrepancy between the nominal and measured values is due to the geometric inconsistencies in 3D printed jigs as well as the slight motion of the fibers inside the resin. The latter is likely associated with cure-induced volumetric changes in the resin which was not characterized in this study. The spatially heterogeneous cure-induced volumetric changes in the epoxy may have caused the slight repositioning of the macro fibers inside the epoxy during the curing process [33]. To ensure the repeatability of experimental measurements, two samples for each (d,α) pair were prepared and tested. All tensile samples were fabricated with a thickness of *ca.* 6 mm.

2.2. Mechanical testing and digital image correlation

The polished surface of the samples was patterned for DIC purposes. Details regarding pattern application and characteristics are provided as **Supplementary Information**. Speckle patterned samples were subjected to uniaxial tensile testing. Tensile tests were performed at a

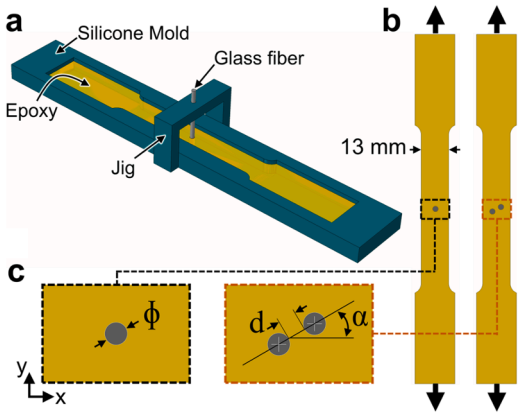

Fig. 1. Schematic of (a) sample preparation process, (b) single and double fiber dog-bone samples, and (c) geometry and relative orientation of the fibers. Tensile sample dimensions were consistent with ASTM D638. Dog bone sample thickness in all cases was ~6 mm.

Table 2-
Sample labels with their corresponding nominal and measured inter-fiber spacing and angular orientation. ϕ, d, and α indicate the fiber diameter (=2 mm), edge-to-edge distance, and inter-fiber angle, respectively. 'FF' in the sample label represents a double-fiber case.

Sample Label	No. of fibers	Inter-fiber distance, d (mm)		Inter-fiber angle, α (°)	
		Nominal	Measured	Nominal	Measured
F	1	–	–	–	–
FF-0.3ϕ–0	2	0.60	0.90 ± 0.26	0	5.44±1.34
FF-1ϕ–0		2.00	1.74 ± 0.24		4.21±1.63
FF-1.5ϕ–0		3.00	2.74 ± 0.11		0.35 ± 0.12
FF-0.3ϕ–30		0.60	0.71 ± 0.15	30	38.79 ± 3.61
FF-1ϕ–30		2.00	1.88 ± 0.23		32.81 ± 1.66
FF-1.5ϕ–30		3.00	2.76 ± 0.05		31.25 ± 1.63
FF-0.3ϕ–45		0.60	0.52 ± 0.06	45	46.66 ± 2.08
FF-1ϕ–45		2.00	1.64 ± 0.18		45.97 ± 0.22
FF-1.5ϕ–45		3.00	2.77 ± 0.12		48.53 ± 1.47
FF-0.3ϕ–60		0.60	0.46 ± 0.06	60	55.14 ± 4.70
FF-1ϕ–60		2.00	2.09 ± 0.21		62.12 ± 2.07
FF-1.5ϕ–60		3.00	2.77 ± 0.18		57.83 ± 2.19
FF-0.3ϕ–90		0.60	0.47 ± 0.01	90	90.64 ± 5.49
FF-1ϕ–90		2.00	1.90 ± 0.12		88.54 ± 1.21
FF-1.5ϕ–90		3.00	2.87 ± 0.09		90.98 ± 0.12

constant crosshead speed of 5 mm/min in a Shimadzu 10 kN universal test frame. A 5 megapixel camera (Basler acA2440–75 μm, 2448 × 2048 px resolution, Germany) equipped with a high magnification macro lens (Tokina atx-i 100 mm macro lens) was used to capture images from the speckled surface of the samples at a rate of 1 Hz. Image acquisition and load-cell data collection rate were synchronized. Images captured during tensile tests were analyzed in the commercial DIC software Vic-2D (Correlated Solutions, Inc., SC, USA) using subset and step sizes of 29 pixels (272 μm) and 7 pixels (65 μm), respectively. The calibration ratio was measured as 9.33 μm/pixel. Full-field strain maps were calculated using Gaussian weighted filter sizes of 5. The combination of the utilized DIC parameters leads to virtual strain gage sizes of *ca.* 330 μm. Considering the ratio between the virtual strain gage size and the fiber diameter, the present work can be considered a scaled-up version of the setup used in [26] to characterize the fiber-matrix interface at micrometric scales.

3. Finite element analysis

Finite element models were created in the commercial software ABAQUS to complement the experimental results obtained from full-

field measurements, while further highlighting the roles of inter-fiber distance and angle in double-fiber samples. 2D geometries replicating those of the single-fiber samples were created. Experimentally determined properties of the individual constituents (see Table 1 and **Supplementary Information**) were assigned to individual constituents, *i.e.*, epoxy matrix and glass macro fiber. The interface between the two components was modeled using the cohesive contact option in ABAQUS. The application of a cohesive interface was justified by the availability of experimental data that allowed for the direct measurement of Mode I traction-separation laws at the fiber-matrix interface. The cohesive contact properties were identified directly from single-fiber tests, as detailed in the **Supplementary Information**.

The most significant outcome of the finite element analyses in this work was the validation of overall strain patterns as well as the study of shear band characteristics. The latter was performed by characterizing the shear band formation patterns in terms of their angle with respect to the loading direction in single-fiber samples. This angle was then used to study the possibility of shear bands coalescence and final matrix failure as functions of inter-fiber spacing and angles in double-fiber samples.

4. Results and discussion

4.1. Single-Fiber samples: Experimental measurements

Fig. 2 shows the evolution of longitudinal strain fields in the vicinity of the glass macro fiber in a single-fiber sample. A narrow high strain band is formed around the fiber at stresses significantly lower than the tensile strength of the epoxy. These narrow high strain bands are initially developed at the upper and lowermost parts of the interface at low global stresses. The development of such high strain bands before debonding is indicative of the deformation localization at the interface vicinity. The localized strain fields developed in these areas will eventually lead to the initiation of the fiber-matrix debonding. At increased stress levels, the high strain band grows further around the glass fiber, shifting from the debonded upper and lowermost parts of the interface towards the intact lateral sides of the fiber. At the same time, a visible separation between the upper and lowermost parts of the fiber and the matrix starts to appear. The development of these debonded zones leads to large openings at the fiber-matrix interface while increasing the level of strain heterogeneity in the matrix and in the vicinity of the fiber-matrix interface. The noticeable asymmetry of strain maps about the vertical axis stems from the slight off-centered location of the fiber in the epoxy dog-bone. An interesting observation in this figure is the value of local strains developed at stresses above 39 MPa. Local strains >0.16 are measured in the matrix prior to failure. These strain values are significantly higher than the failure strain of the epoxy, as reported in Table 1. Detailed examination of the fiber-matrix area at stresses just before complete failure reveals the presence of microcracks at the same locations wherein high strain bands are formed. As shown in Fig. 3, evidence for such microcracks was observed in single-fiber samples at global stresses >39 MPa. The strain fields associated with these microcracks are so highly localized that the high magnification optical DIC was unable to capture their location and region of influence. Instead, their collective effect on the deformation and failure of single-fiber samples was revealed in the form of shear band zones formed at certain angles around the fiber.

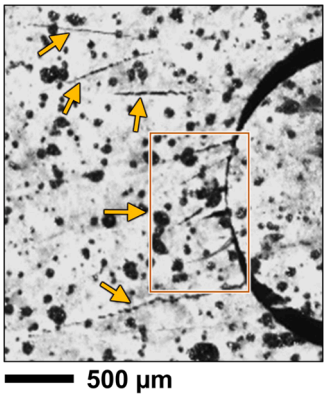

Fig. 3. Evidence of matrix microcracks (marked by arrows) developed in single-fiber samples at global stresses above 39MPa.

Stages of debond propagation that leads to the complete failure of the matrix (at 41 MPa) are presented in Fig. 4. The visual characteristics of the debond initiation and growth in the single-fiber sample are in good agreement with the theory of fiber-matrix interfacial debond [2, 9] and resemble the observations made on single glass fiber samples at significantly smaller length scales [26]. Fig. 4 also shows the angular location of the matrix crack that led to complete matrix failure. Prior analytical and modeling studies predict that the matrix crack nucleation occurs at an angle $<90°$ relative to the load direction [9]. While the experimental observations in this work are consistent with such predictions, we are not certain whether the oblique-angled failure location (marked at 10.3° relative to the horizontal) is a direct consequence of the mechanics of the problem, as predicted by previous analytical studies, or it is due to the slight off-centered location of the glass macro fiber that gives rise to asymmetric deformation patterns. Nonetheless, the full-field nature of strain measurements in this work allows for further quantitative analysis of local deformation and failure in single fiber samples. Specifically, the

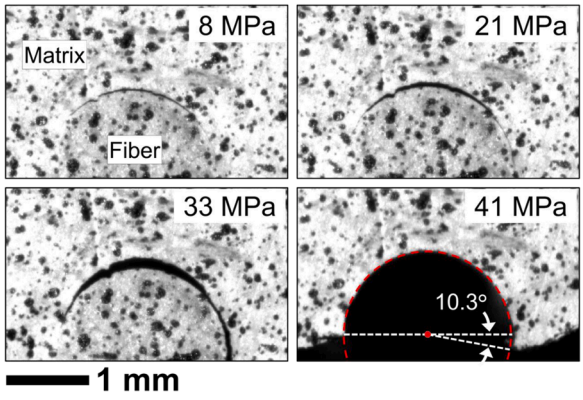

Fig. 4. Various stages of fiber-matrix debond evolution in a single-fiber sample. Matrix occurred at 41 MPa. Dotted lines on the lower right image mark the location of the glass macro fiber and the angle of matrix crack nucleation point.

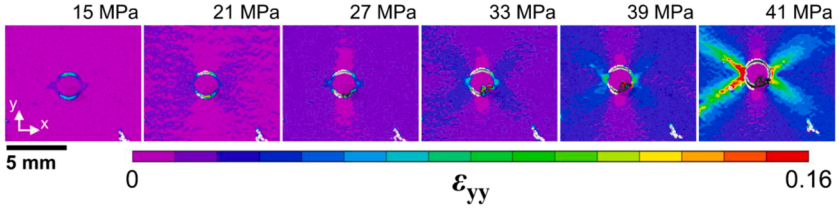

Fig. 2. Evolution of longitudinal strain field (ε_{yy}) in the vicinity of a single glass macro fiber at various global stresses. Tensile load was applied in *y*-direction.

sub-pixel resolution of deformation and strain measurements by DIC allows for the quantitative characterization of debonding-induced opening at the interface with resolutions beyond those conducted by pixel counting [31].

Fig. 5 shows the evolution of local strains and interface opening displacements extracted from various locations around the fiber and across the fiber-matrix interface. The local strain curves in Fig. 5a are extracted from 500 × 500 μm^2 squared regions located 250 μm away from the interface. Local strain curves extracted from representative locations L and R show a constant increase with increasing stress. Interestingly, the strain data extracted from T and B locations show an initial increase up to global stress of *ca.* 5 MPa (marked by the blue arrow in Fig. 5a inset). The curves then show a noticeable decrease which is again followed by another gradual increase that continues until sample failure. The strain decrease at ~5 MPa is due to the partial unloading of the matrix that occurs due to the initiation of the interface debond. This interface debond nucleates symmetrically from diagonally opposite locations at the upper and lowermost parts of the interface. The symmetry in the debond formation is confirmed by tracking the local interfacial openings shown in Fig. 5b. Another noteworthy observation in Fig. 5b is the clear change of slope in the interface opening curves at global stress of *ca.* 5 MPa. This stress level is the same as that wherein the strain peaks were observed in Fig. 5a. Besides providing a unique insight into the multiscale deformation and failure response in single-fiber samples, the experimental measurements in Fig. 5 were used to calibrate traction-separation laws necessary for the finite element analyses in this work. Calibration of traction-separation law along with details of the finite element modeling approach is presented as **Supplementary Information**.

4.2. Single-Fiber samples: finite element analysis

Fig. 6 shows a comparison between strain fields in the single-fiber samples obtained from DIC and finite element analysis. The contour maps in this figure show the distribution of in-plane normal and shear strain components. To replicate the geometric characteristics of the experimental measurements, the location of the glass macro fiber was intentionally chosen to be slightly off-center in our FE models. The qualitative agreement between the experimental and model-predicted results is notable. The modeling results capture the deformation patterns characterized by DIC measurements. The orientation of the highly localized strain bands shown in ε_{yy} and ε_{xx} maps is directly marked on the contour maps and is measured to be 37° relative to the horizontal. These highly strained bands coincide with angles at which maximum shear strain is developed. Therefore, the high strain bands are representative of strong shear deformations developed around the fiber-matrix interface and are hereafter referred to as *shear bands*. As discussed in the following, the so-called shear bands are nucleation sites for matrix microcracks. In addition, as described later, the coalescence of these shear bands drives the propensity of crack coalescence between the nearest fibers.

4.3. Double-Fiber samples: strain fields

Fig. 7 shows the evolution of experimentally measured strain fields in double-fiber samples. This figure shows the evolution of longitudinal strains in double-fiber samples with the nominal inter-fiber spacing of 1ϕ (see Table 2). The experimental results shown in this figure are consistent with the model predictions of Sandino *et al.* [15]. Previous modeling results suggest that in double-fiber composites, when the two fibers are positioned perpendicular to the direction of the load (*i.e.,* $\alpha = 0°$), debond and failure mechanisms coincide with those of the single-fiber cases. As such, the deformation field and the interfacial debond of one fiber will have minimal effect on those of the other fiber. This trend is observed in Fig. 7a wherein strain patterns developed around either of the fibers resemble those observed for single-fiber samples (see Fig. 2). In conditions where $30° \leq \alpha \leq 60°$, *i.e.*, Fig. 7b-d, a clear interaction between the strain fields is observed. These interactions are developed in the form of a single highly localized strain band that connects the two fibers at the shortest distance. Finally, in cases where the two fibers are aligned with the external load direction, *i.e.*, Fig. 7e, no particular interaction can be observed between the two fibers, at least qualitatively.

4.4. Double-Fiber samples: Fiber interaction

Most previous analytical and computational investigations suggest that in the case of multiple fiber samples, a quantitative evaluation of fiber interaction mechanisms is possible through the determination of the energy release rate. The energy release rate calculations require information about the local strain as well as local stress fields. While the former is directly obtainable from DIC, experimental measurement of local stress fields is not practically possible. Therefore, in this work, instead of correlating failure patterns with energy release rate, we examine the debond and matrix failure patterns in terms of deformation and strain fields developed in the vicinity of neighboring fibers.

As the first step in this process, the debond symmetry in double fiber samples is investigated. Fig. 8 shows the evolution of interface opening displacement at the upper and lowermost areas across the fiber-matrix interface in double-fiber samples. Note that the data presented in this figure only include samples whose nominal fiber spacing is roughly equal to 1 fiber diameter, *i.e.,* $d = 1\phi$. As described earlier, for $\alpha = 0°$ a symmetric debond-induced opening displacement is observed. The interface opening displacements, in this case, are also close to those measured for single fiber samples (Fig. 5b). This observation is consistent with previous modeling studies wherein the effect of neighboring fibers on debond initiation is shown to be minimal when the nearby fibers are positioned perpendicular to the direction of the tensile load, *i.*

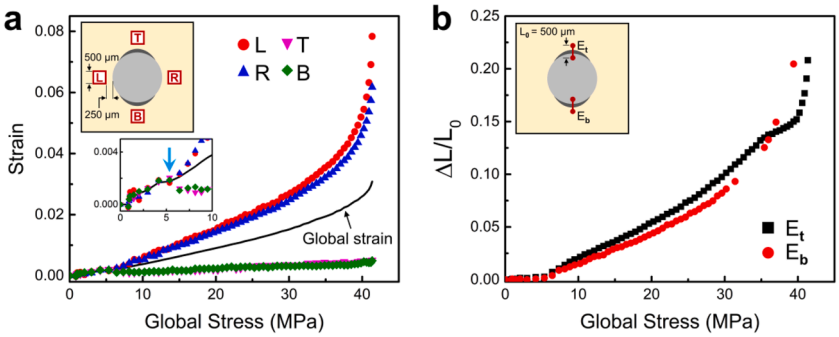

Fig. 5. (a) Variation of local strain fields extracted from four representative locations around the fiber. The representative locations are selected at the top, T, bottom, B, right, R, and left, L, of the fiber. Global strain curve is plotted for reference. (b) Evolution of interface opening at the upper and lowermost positions at the interface. Opening extensions are measured using 500 μm (~54 pixels) virtual extensometers, Et and Eb.

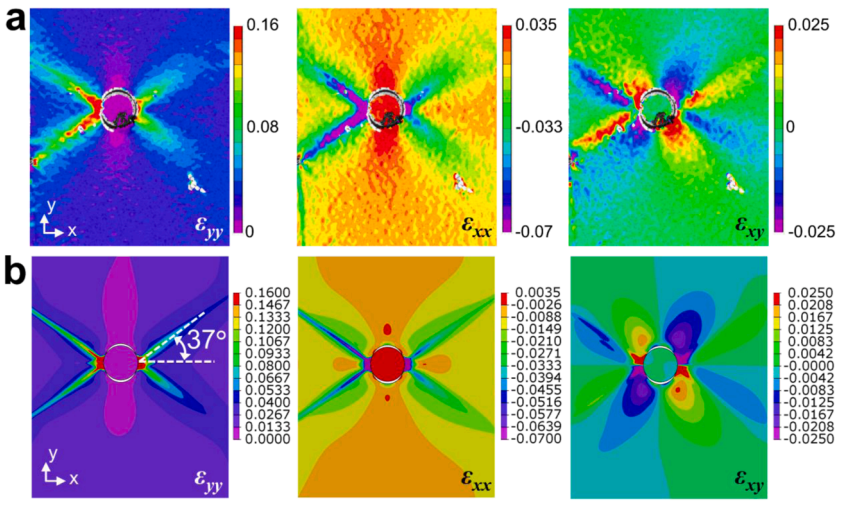

Fig. 6. Comparing in-plane strain fields (normal: ε_{yy}, ε_{xx} and shear: ε_{xy}) developed around the glass macro fiber in a single-fiber sample obtained from (a) DIC and (b) FEA.

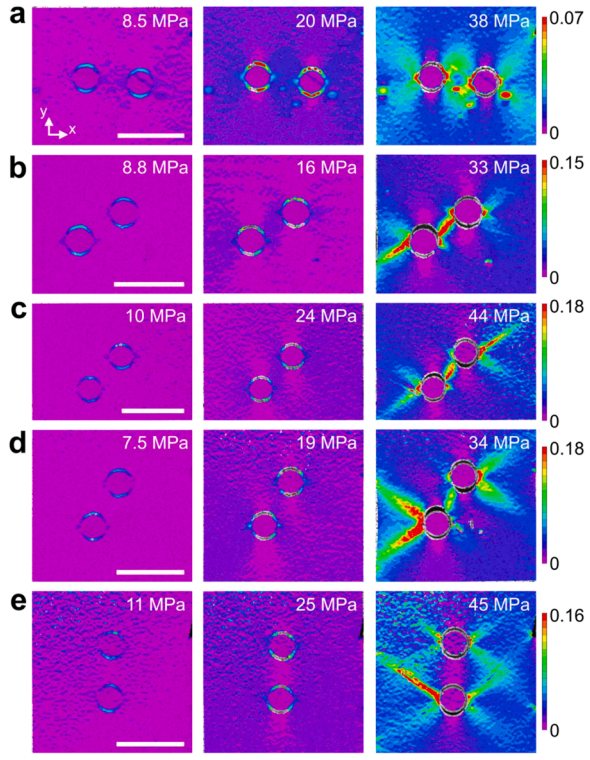

Fig. 7. Evolution of longitudinal strain fields (ε_{yy}) at various global stresses and in the vicinity of double glass fiber samples: (a) FF-1ϕ−0, (b) FF-1ϕ−30, (c) FF-1ϕ−45, (d) FF-1ϕ−60, and (e) FF-1ϕ−90. The contour maps on the right column are extracted at global stresses just before matrix failure in all cases. Scale bar: 5 mm.

e., $\alpha = 0°$. In contrast, for $\alpha > 0°$, a clear asymmetry in the interface opening displacement curves is observed. Interestingly, for $\alpha = 45°$, a remarkable symmetric response is observed up to the global stress of *ca.* 40 MPa. Another noteworthy observation is the rate at which the opening displacement curves evolve at low global stresses. This rate can be qualitatively characterized by considering the insets shown in Fig. 8. The initial rate of displacement increase is observed to be higher for $\alpha = 60°$ and 90°. This observation is also in agreement with previous modeling analyses and is related to the lower levels of tensile load required to initiate debond propagation [15]. Last but not least, the maximum opening displacements achieved in each case prior to complete matrix failure are dependent on the inter-fiber angle, α. The maximum opening displacement is measured to be the lowest for $\alpha = 0°$ and 90° and highest for $\alpha = 30°$ and 60°. For $\alpha = 45°$, the maximum opening displacement before matrix failure is somewhat between the two extreme values, but closer to those of $\alpha = 60°$. Complementary data regarding the tensile strength of dog-bone samples with one and two fibers and the relevant information are provided as **Supplementary Information**.

The combined effects of interface debond nucleation and propagation can be manifested in the matrix failure patterns. In particular, the matrix crack propagation angles in areas confined between the two fibers can provide crucial information on the potential effects of fiber interactions in response to a remote tensile load. Fig. 9 shows post-mortem matrix crack angles for various samples. This figure compares the failure patterns for double-fiber samples with short and long inter-fiber distances. The short and long inter-fiber distance in this figure refer to the smallest and largest fiber spacings examined in this work (see Table 2). In general, for all short inter-fiber cases (left column figures in Fig. 9), the measured matrix failure angle is the same as the initial angular distance between the two fibers. This behavior is consistent with the assumption of crack linking between the nearest-neighbor fibers [13–15]. However, failure patterns in Fig. 9d,e show a clear divergence from the previous observations, indicating a horizontal matrix failure. In these two cases, *i.e.*, samples FF-1.5ϕ−60 and FF-1.5ϕ−90, the matrix failure has initiated from the bottom fiber and propagated with minimal interference from the top fiber.

To explore the reasons behind the aforementioned anomalies observed for $\alpha = 60°$ and 90°, the evolution of shear strain fields between the two fibers was examined. Fig. 10 shows the development of local shear strain fields in a sample with $\alpha = 30°$ and an initial fiber distance of *ca.* 2 mm, *i.e.*, $d = 1\phi$. Local shear strain fields formed at diagonally opposite areas around the interface. At stresses above 30 MPa, the shear deformation zones are shown to develop more rapidly. The coalescence of these shear bands occurs at >30 MPa in the form of a highly deformed strip that connects the two fibers at the shortest distance. As shown in Fig. 10b, matrix microcracks initiate at the location of and along the direction of these highly localized shear bands.

The above observations allow us to assume that the coalescence of shear bands that develop at certain angles around the fibers (Fig. 6) eventually leads to matrix failure in the case of multiple fiber samples. However, whether such coalescence is dependent on the distance and angle of the nearest fibers is still unclear. To address this question, a simple analysis based on the assumption of 37° shear bands (see Fig. 6

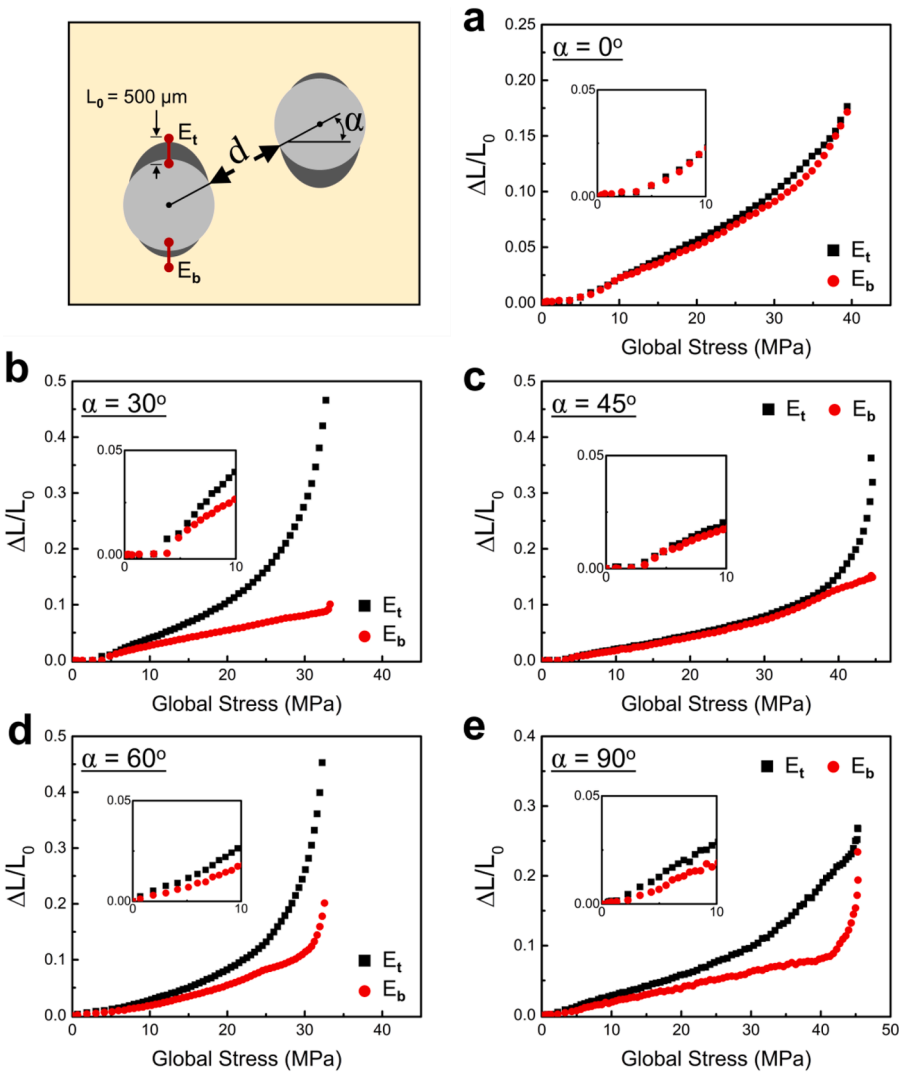

Fig. 8. Evolution of normal opening extension ($\Delta L/L_0$) extracted from the upper, E_t, and lowermost, E_b, parts of the fiber-matrix interface. For clarity, data from the left fiber are only provided. Data shown for (a) FF-1ϕ−0, (b) FF-1ϕ−30, (c) FF-1ϕ−45, (d) FF-1ϕ−60, and (e) FF-1ϕ−90.

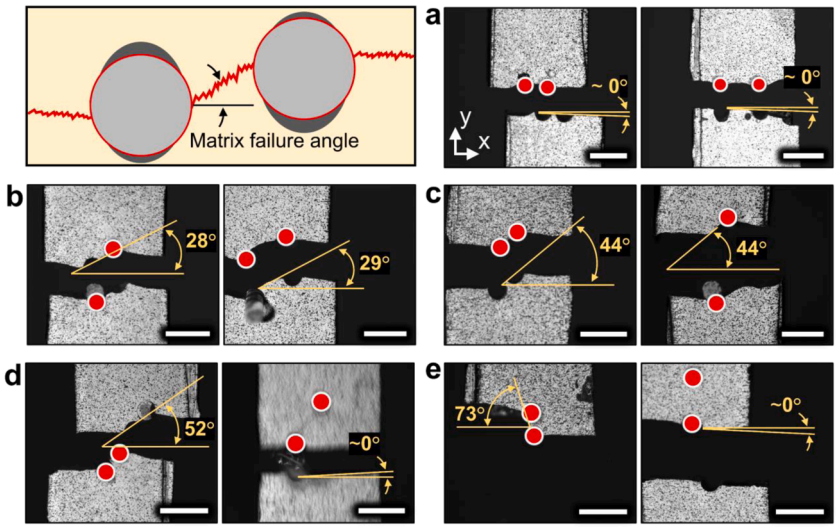

Fig. 9. Postmortem matrix failure angle measurements for double-fiber samples with short (left column) and long (right column) inter-fiber spacings. Data shown for samples with (a) $\alpha = 0°$, (b) $\alpha = 30°$, (c) $\alpha = 45°$, (d) $\alpha = 60°$, and (e) $\alpha = 90°$. Red circles indicate the original locations of the fibers. Scale bar: 5 mm.

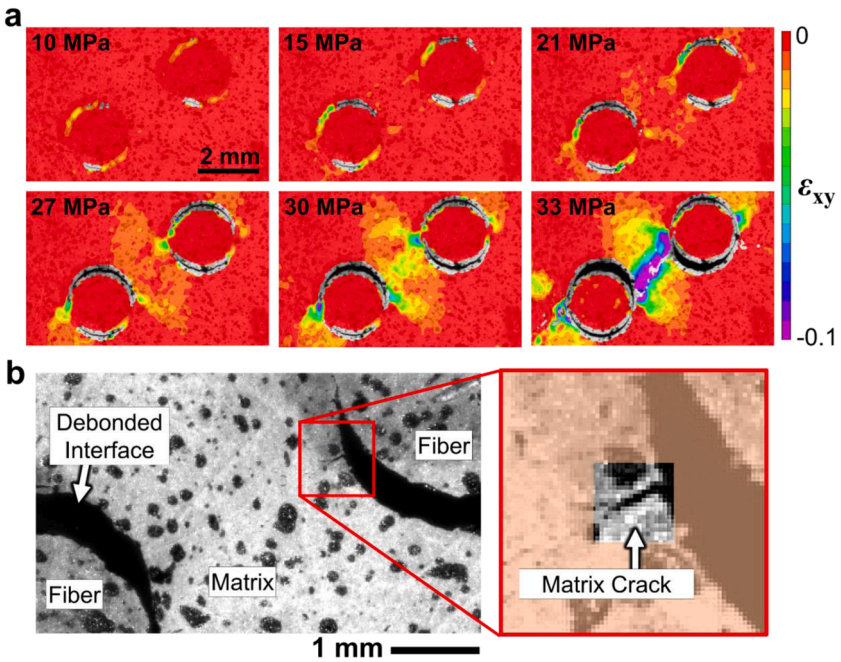

Fig. 10. (a) Evolution of local shear strain fields in FF-1ϕ−30 at various global stresses. (b) A magnified view of the epoxy ligament between the two fibers, showing the location of matrix crack initiation.

and **Supplementary Information**) was conducted. In this analysis, the normal distance between the trajectory of the shear bands and the inter-fiber distance was first established. Fig. 11a shows the schematic of the geometric features of this analysis. The correlations between shear band distance, L, and the inter-fiber distance are shown as a color map in Fig. 11b. The negative values in this color map refer to cases where the angle between the two fibers is smaller than the shear band angle, *i.e.,* $\alpha < 37°$. Next, through postmortem matrix failure measurements (like those shown in Fig. 9), samples in which shear band coalescence was observed were separated from those in which the matrix failure occurred with no apparent interactions between the two fibers. The (α,d) pairs associated with these observations are overlayed directly on Fig.11b and distinguished with solid and hollow circles, respectively. Interestingly, matrix crack coalescence was observed for all inter-fiber angles at all examined d/ϕ ratios <0.5. At larger d/ϕ ratios, the possibility of shear band coalescence was found to be strongly dependent on the inter-fiber angle. A clear distinction between the two sets of data points seems to have been established at $\alpha > 45°$ and inter-fiber distances larger than one fiber diameter, *i.e.,* $d/\phi > 1$. While not explored in the present work, we anticipate that the latter observations may be directly correlated with the interactions between the plastic zones and stress concentration fields between two neighboring cracks [34, 35]. Nonetheless, the experimental results obtained in this work point to the fact that the assumption of the crack linking and coalescence between the nearby fibers may not always be realistic. As such, more accurate analyses of transverse cracking and matrix failure in UD composites require detailed information about the distance and angle between the so-called nearby neighbors, especially in the analysis of composites with dilute fiber packings [36]. Unlike composites with high fiber volume fractions wherein fibers are densely packed, in dilute fiber packing conditions, the neighboring fibers may be located further away from each other. In such conditions, the fiber interaction mechanisms discussed in this work can provide a useful insight into the origin of transverse failure in the composite sample.

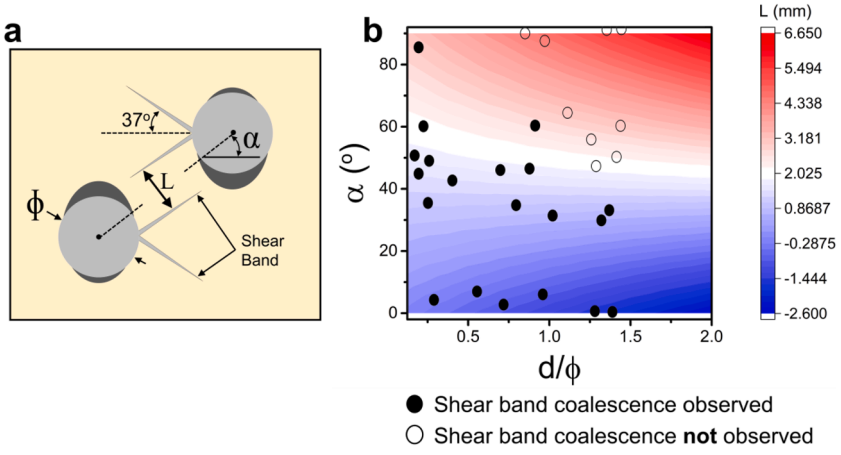

Fig. 11. (a) Schematic of the geometric features of the shear band coalescence analysis, sowing the normal distance between the trajectory of the shear bands, denoted by L. (b) The correlations between L, α, and d/ϕ ratio shown as by the color map. The (α,d/ϕ) pairs wherein the coalescence of shear bands were observed (or not observed) are shown by the overlayed black or hollow circles.

5. Current limitations and future directions

Although the presented results and discussions provide an insight into the fiber interaction mechanisms from an experimental perspective, it is important to understand the limitations of the current measurement approach. The most significant limitation of the implemented approach is its inability to provide an insight into the out-of-plane deformation behavior of the matrix in the vicinity of the fibers. While it is believed that owing to the relatively low ductility of the matrix, such out-of-plane strains would have minimal effect on the strain measurements [37], a more accurate assessment of the local deformation fields requires the inclusion of out-of-plane displacements and strains as well. This issue can be addressed by performing high magnification stereo DIC measurements similar to those described in [29, 38].

Another limitation of the current study originates from the application of unsized macro fibers. The unsized glass macro fibers used in this study led to weak fiber-matrix interface strengths [39]. The consequence of such weak interfaces is manifested in the lack of concrete evidence for crack kink-out mechanisms. Additionally, the lack of sizing on glass macro fibers raises the question that whether the observed interface debonding represents real composites wherein the fiber sizing plays a significant role in the debonding mechanisms. While the fiber sizing issue is recognized as a limitation of the present work, it can also be an interesting topic of research for future studies. Research is currently underway to further explore the role of interface conditions by comparing unsized and silane surface treated glass macro fibers. It is expected for the treated fibers to show significantly larger debond initiation strain and stresses [39].

Finally, the uncertainties caused by the imprecise alignment of the fibers in the matrix challenge the surface measurements by DIC and their application in the validation of FE models. Efforts are underway to address this limitation by simultaneous measurement of surface and through-thickness deformation and failure behaviors in similar composite systems. Through-thickness characterizations would be possible due to the transparent nature of the epoxy system used in this work. Furthermore, the off-centered and asymmetric placement of the macro fibers relative to the direction of the external load is another interesting topic of future research that will enable the investigation of mixed-mode fiber-matrix debonding behavior in composites.

6. Conclusions

The effects of inter-fiber distance and angle on the interactions between two nearby fibers were analyzed by full-field experimental measurements. Single and double-fiber samples were fabricated using glass macro fibers embedded in an epoxy matrix. Induced by the application of far-field tensile stresses, strain fields developed in the vicinity of the fibers were characterized using high magnification optical digital image correlation. Global and local deformation responses in single-fiber samples were evaluated first. The results of these analyses were used to calibrate a finite element model as well as to understand the deformation patterns in the neighborhood of a fiber subjected to transverse tension. This information was then used to investigate the fiber-matrix debond and matrix failure mechanisms in double-fiber samples. It was revealed that the coalescence of shear bands initiated from the fiber-matrix interface in nearby fibers attributes to the inter-fiber matrix failure in closely packed composites. This shear band coalescence mechanism was found to be dependent on the distance and angle between two neighboring fibers. Finally, it was shown that the shear band coalescence and inter-fiber matrix cracking are less likely to occur when the nearest fibers are distanced further than one fiber diameter apart and positioned at an angle $<45^{\circ}$ relative to the tensile load direction. The experimental approach developed here can be utilized to study the fiber interaction mechanisms and their consequence on transverse cracking behavior in composites made from various fiber-matrix systems.

Supplementary information

Details regarding DIC speckle pattern application and characteristics, mechanical testing of the neat epoxy matrix, sample preparation practice, Identification of traction-separation laws, finite element analysis, and tensile strength measurement are provided as Supplementary Information.

Data availability

Data (including DIC images and raw experimental measurement data) will be available upon request.

Declaration of Competing Interest

The authors declare no conflict of interest.

Acknowledgments

B.K. gratefully acknowledges the financial support from the Advanced Materials and Manufacturing Institute (AMMI) at Rowan University. This work was partially supported by Rowan University faculty start-up funds.

Supplementary materials

Supplementary material associated with this article can be found, in the online version, at doi:10.1016/j.jcomc.2022.100229.

References

[1] R. Talreja, Transverse cracking and stiffness reduction in composite laminates, J. Compos. Mater. 19 (1985) 355–375.
[2] L. Zhuang, R. Talreja, J. Varna, Transverse crack formation in unidirectional composites by linking of fibre/matrix debond cracks, Compos. Part A 107 (2018) 294–303.
[3] F. Paris, E. Correa, V. Mantic, Kinking of transversal interface cracks between fiber and matrix, J. Appl. Mech. 74 (2007) 703–716.
[4] W. Tan, F. Naya, L. Yang, T. Chang, B.G. Falzon, L. Zhan, J.M. Molina-Aldareguia, C. Gonzalez, J. Llorca, The role of interfacial properties on the intralaminar and interlaminar damage behaviour of unidirectional composite laminates: experimental characterization and multiscale modelling, Compos. Part B 138 (2018) 206–221.
[5] M.L. Velasco, E. Graciani, L. Tavara, E. Correa, F. Paris, BEM multiscale modelling involving micromechanical damage in fibrous composites, Eng. Anal. Bound. Elem. 93 (2018) 1–9.
[6] M.L. Velasco, E. Correa, F. París, Interaction between fibres in the transverse damage in composites, Eng. Fract. Mech. 239 (2020), 107273.
[7] Shakiba M., Brandyberry D.R., Zacek S., Geubelle P.H., Transverse failure of carbon fiber composites: analytical sensitivity to the distribution of fiber/matrix interface properties. 2019; 120: 650–665.
[8] X. Zhang, D.R. Brandyberry, P.H. Geubelle, IGFEM-based shape sensitivity analysis of the transverse failure of a composite laminate, Comput. Mech. 64 (2019) 1455–1472.
[9] I.G. Garcia, V. Mantic, E. Graciani, Debonding at the fibre-matrix interface under remote transverse tension. One debond or two symmetric debonds? Eur. J. Mech. A/Solids 53 (2015) 75–88.
[10] F. Sharifpour, J. Montesano, R. Talreja, Assessing the effects of ply constraints on local stress states in cross-ply laminates containing manufacturing induced defects, Compos. Part B 199 (2020), 108227.
[11] S.A. Elnekhaily, R. Talreja, Damage initiation in unidirectional fiber composites with different degrees of nonuniform fiber distribution, Compos. Sci. Technol. 155 (2018) 22–32.
[12] M. Hojo, M. Mizuno, T. Hobbierbrunken, T. Adachi, M. Tanaka, S.K. Ha, Effects of fiber array irregularities on microscopic interfacial normal stress states of transversely loaded UD-CFRP from viewpoint of failure initiation, Compos. Sci. Technol. 69 (2009) 1726–1734.
[13] N. Vejen, R. Pyrz, Transverse crack growth in glass/epoxy composites with exactly positioned long fibres. Part I: experimental, Compos. Part B 32 (7) (2001) 557–564.
[14] L. Zhuang, A. Pupurs, J. Varna, R. Talreja, Z. Ayadi, Effects of inter-fiber spacing on fiber-matrix debond crack growth in unidirectional composites under transverse loading, Compos. Part A 109 (2018) 463–471.
[15] C. Sandino, E. Correa, F. Paris, Numerical analysis of the influence of a nearby fibre on the interface crack growth in composites under transverse tensile load, Eng. Fract. Mech. 168 (2016) 58–75.

[16] S. Zhandarov, E. Mäder, Characterization of fiber/matrix interface strength: applicability of different tests, approaches and parameters, Compos. Sci. Technol. 65 (2005) 149–160.
[17] C. Ageorges, K. Friedrich, T. Schüller, B. Lauke, Single-fibre Broutman test: fibre-matrix interface transverse debonding, Compos. Part A 30 (1999) 1423–1434.
[18] J.-.M. Chu, B. Claus, N. Parab, D. O'Brien, T. Sun, K. Fazzaa, W. Chen, Visualization of dynamic fiber-matrix interfacial shear debonding, J. Mater. Sci. 53 (2018) 5845–5859.
[19] S. Tamrakar, R. Ganesh, S. Sockalingam, J.W. Gillespie Jr., Rate dependent mode II traction separation laws for S-2 glass/epoxy interface using a microdroplet test method, Compos. Part A 124 (2019), 105487.
[20] K. Martyniuk, B.F. Sorensen, P. Modregger, E.M. Lauridsen, 3D *in situ* observations of glass fiber/matrix interfacial debonding, Compos. Part A 55 (2013) 63–73.
[21] W. Zhang, A. de, L.G. Melo, A.P. Hitchcock, N. Bassim, Electron beam damage of epoxy resin films studied by scanning transmission X-ray spectromicroscopy, Micron 120 (2019) 74–79.
[22] A. Rashidi, T. Olfatbakhsh, B. Crawford, A.S. Milani, A review of current challenges and case study toward optimizing micro-computed X-ray tomography of carbon fabric composites, Materials (Basel) 13 (2020) 3606.
[23] J. Tracy, S. Daly, K. Sevener, Multiscale damage characterization in continuous fiber ceramic matrix composites using digital image correlation, J. Mater. Sci. 50 (2015) 5289–5299.
[24] B. Koohbor, S. Ravindran, A. Kidane, A multiscale experimental approach for correlating global and local deformation response in woven composites, Compos. Struct. 194 (2018) 328–334.
[25] B. Koohbor, S. Ravindran, A. Kidane, Meso-scale strain localization and failure response of an orthotropic woven glass-fiber reinforced composite, Compos. Part B 78 (2015) 308–318.
[26] C.B. Montgomery, B. Koohbor, N.R. Sottos, A robust patterning technique for electron microscopy-based digital image correlation at sub-micron resolution, Exp. Mech. 56 (2019) 1063–1073.
[27] M. Mehdikhani, M. Aravand, B. Sabuncuoglu, M.G. Callens, S.V. Lomov, L. Gorbatikh, Full-field strain measurements at the micro-scale in fiber-reinforced composites using digital image correlation, Compos. Struct. 140 (2016) 192–201.
[28] Koohbor B., Montgomery C.B., White S.R., Sottos N.R., Meso-scale Strain Measurements in Fiber Reinforced Composites. 33rd Technical Conference of the American Society for Composites 2018; Seattle, WA, USA. DOI 10.12783/asc33/26028 (http://www.dpi-proceedings.com/index.php/asc33/article/view/26028).
[29] I. Tabiai, R. Delorme, D. Therriault, M. Levesque, In-situ full field measurements during inter-facial debonding in single fiber composites under transverse load, Exp. Mech. 58 (2018) 1451–1467.
[30] I. Tabiai, D. Texier, P. Bocher, D. Therriault, M. Levesque, In-situ full field out of plane displacement and strain measurements at the micro-scale in single reinforcement composites under transverse load, Exp. Mech. 60 (2020) 359–377.
[31] I. Tabiai, G. Tkachev, P. Diehl, S. Frey, T. Ertl, D. Therriault, M. Levesque, Hybrid image processing approach for autonomous crack area detection and tracking using local digital image correlation results applied to single-fiber interfacial debonding, Eng. Fract. Mech. 216 (2019), 106485.
[32] T.J. Vaughan, C.T. McCarthy, Micromechanical modelling of the transverse damage behaviour in fibre reinforced composites, Compos. Sci. Technol. 71 (3) (2011) 388–396.
[33] O.G. Kravchenko, S.G. Kravchenko, A. Casares, R.B. Pipes, Digital image correlation measurement of resin chemical and thermal shrinkage after gelation, J. Mater. Sci. 50 (2015) 5244–5252.
[34] S.H. Song, B.H. Choi, Effect of plastic zone on the fatigue crack propagation behavior between two fatigue cracks, Exp. Mech. 41 (2001) 225–231.
[35] J. Koivisto, M.J. Dalbe, M.J. Alava, S. Santucci, Path (un)predictability of two interacting cracks in polycarbonate sheets using digital image correlation, Sci. Rep. 6 (2016), 322278.
[36] V. Mantič, L. Távara, A. Blázquez, E. Graciani, F. París, A linear elastic-brittle interface model: application for the onset and propagation of a fibre-matrix interface crack under biaxial transverse loads, Int. J. Fracture 195 (2015) 15–38.
[37] M.A. Sutton, J.H. Yan, V. Tiwari, H.W. Schreier, J.J. Orteu, The effect of out-of-plane motion on 2D and 3D digital image correlation measurements, Opt. Lasers Eng. 46 (10) (2008) 746–757.
[38] B. Koohbor, S. Ravindran, A. Kidane, Experimental determination of Representative Volume Element (RVE) size in woven composites, Opt. Lasers Eng. 90 (2017) 59–71.
[39] J.L. Thomason, Glass fibre sizing: a review, Compos. Part A 127 (2019), 105619.